Matter

CellPress

Article

Colloidal synthesis and charge carrier dynamics of $Cs_4Cd_{1-x}Cu_xSb_2Cl_{12}$ ($0 \leq x \leq 1$) layered double perovskite nanocrystals

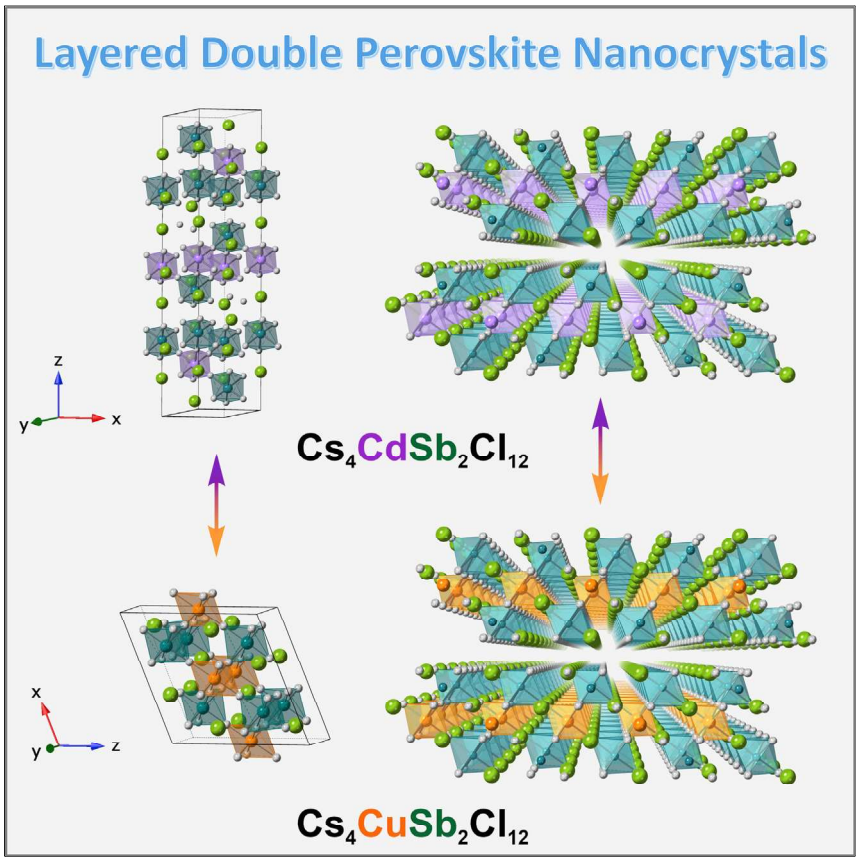

Colloidal synthesis of a series of $Cs_4Cd_{1-x}Cu_xSb_2Cl_{12}$ layered double perovskite nanocrystals is achieved. The composition-structure-property relationships of the resultant nanocrystals are studied through materials characterization, density functional theory calculations, and transient-absorption spectroscopy. Colloidal NCs can be solution processed into a high-speed photodetector, demonstrating their potential in optoelectronic applications.

Tong Cai, Wenwu Shi, David J. Gosztola, ..., Jianbo Gao, Xuedan Ma, Ou Chen

ouchen@brown.edu

Highlights

Colloidal $Cs_4CdSb_2Cl_{12}$ LDP NCs are synthesized

Composition-structure-property relations are demonstrated using $Cs_4Cd_xCu_{1-x}Sb_2Cl_{12}$ NCs

$Cs_4CdSb_2Cl_{12}$ and $Cs_4CuSb_2Cl_{12}$ LDP NCs show different charge carrier dynamics

Colloidal $Cs_4CdSb_2Cl_{12}$ LDP NCs are solution processed into high-speed photodetectors

3 Understanding
Dependency and conditional studies on material behavior

Cai et al., Matter 4, 2936–2952
September 1, 2021
https://doi.org/10.1016/j.matt.2021.07.018

CellPress

Matter

Article

Colloidal synthesis and charge carrier dynamics of $Cs_4Cd_{1-x}Cu_xSb_2Cl_{12}$ ($0 \leq x \leq 1$) layered double perovskite nanocrystals

Tong Cai,[1] Wenwu Shi,[1,2] David J. Gosztola,[3] Kanishka Kobbekaduwa,[4] Hanjun Yang,[1] Na Jin,[1] Yasutaka Nagaoka,[1] Lacie Dube,[1] Jeremy Schneider,[1] Sooyeon Hwang,[5] Jianbo Gao,[4] Xuedan Ma,[3] and Ou Chen[1,6,*]

SUMMARY

The toxicity and instability of lead-based metal halide perovskites are the two main obstacles that prevent perovskite materials from implementation in applications. Recently, layered double perovskites (LDPs) have emerged as a new family of perovskite materials, which provide a new route to solve these problems by lead-component replacement and reduction of crystal structure dimensionality. However, LDP nanocrystals (NCs) have been rarely studied, limiting the further property exploration and application realization. Here, we report the colloidal synthesis of a series of $Cs_4Cd_{1-x}Cu_xSb_2Cl_{12}$ ($0 \leq x \leq 1$) LDP NCs by tuning the stoichiometry of metal precursors. The composition-structure-property relationships of the resulting LDP NCs are studied through material characterizations, density functional theory calculations, and transient-absorption spectroscopy. In addition, we demonstrate that high-performance high-speed photodetectors can be fabricated using the colloidal LDP NCs through solution processing. This work premises further expansion of such LDP-based materials for both fundamental studies and application integrations.

INTRODUCTION

Three-dimensional (3D) metal halide perovskite (MHP) nanocrystals (NCs) with a general formula of $AM(II)X_3$ (A: Cs, methylammonium, formamidinium, etc.; M: Pb, Sn, Ge, etc.; X: Cl, Br, I) have aroused tremendous research interest owing to their marvelous tunability in structural, optical, and (opto)electronic properties in response to targeted applications such as solar cells,[1,2] light-emitting diodes,[3–5] X-ray scintillators,[6] lasing,[7] luminescent solar concentrators,[8–10] photocatalysis,[11,12] etc.[13–15] However, limited choices for M(II) in the general formula of $AM(II)X_3$ MHPs and the intrinsic instability issue of the materials hinder their potentials in a wide range of practical implementations. To alleviate these problems, multiple strategies toward compositional expansion of MHPs have proven to be effective and beneficial from material design, structure/property tuning, long-term stability, and application-integration points of view.[16–18] For instance, the divalent M(II) component can be substituted by other heterovalent metal elements, resulting in a library of 3D lead-free perovskite derivatives, including, e.g., 3D $Cs_2M(I)M(III)X_6$ double perovskites (DPs) and vacancy-ordered $Cs_2M(IV)X_6$ perovskites.[19–26] The same lead replacement strategy can also address the instability issue of lead-based MHPs by the reduction of structural dimensionality to, e.g., 2D $Cs_3M(III)_2X_9$ layered

Progress and potential

Metal halide perovskite nanocrystals (NCs) have attracted tremendous attention due to their unique crystal structure and promising optoelectronic properties. Particularly, layered double perovskite (LDP) NCs with enriched compositional space and highly tunable properties are important for both fundamental studies and technological applications. Here, we report the colloidal synthesis of a series of $Cs_4Cd_{1-x}Cu_xSb_2Cl_{12}$ ($0 \leq x \leq 1$) LDP NCs with controlled metal compositions. Insights on the composition-structure-property relationships of the LDP NCs are explored through both material characterizations and theoretical calculations. Photogenerated charge carrier dynamics of the LDP NCs are investigated using ultrafast spectroscopic techniques. We show that such colloidal LDP NCs can be solution processed into a high-speed photodetector, demonstrating their potential in applications such as optical, photonic, and optoelectronic devices.

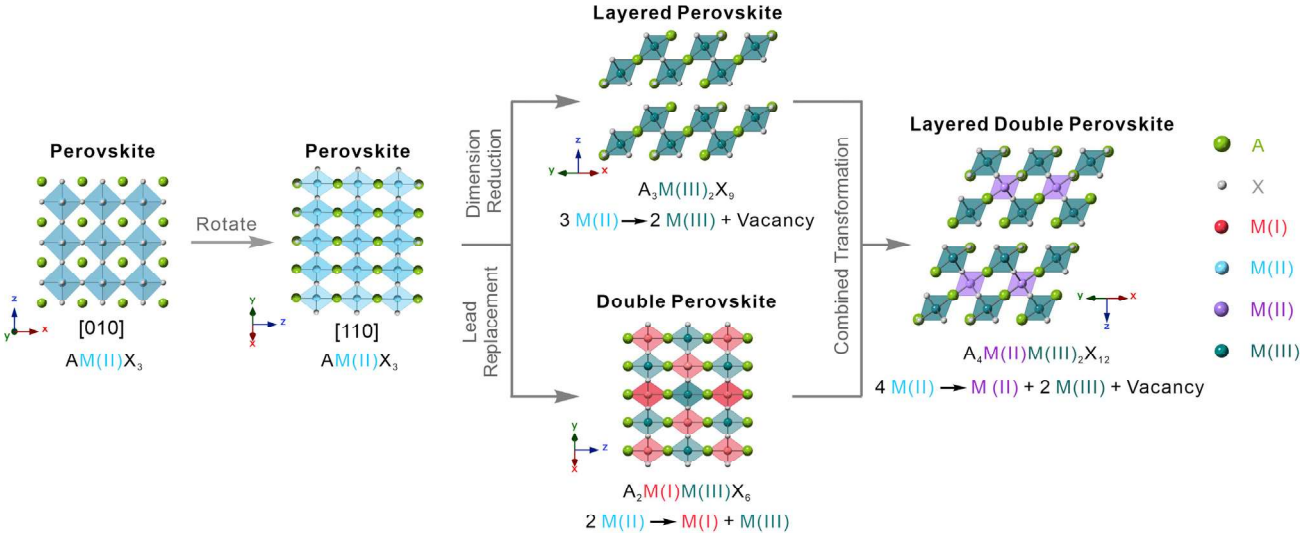

Scheme 1. Schematic of the evolution of metal halide perovskites from the conventional 3D perovskite to layered double perovskite crystal structure

perovskites (LPs) and 0D $Cs_3M(III)X_6$ perovskites, without sacrificing the tunability of materials' composition and properties.[27–30] By combining the lead element replacement and crystal dimensionality reduction strategies, all-inorganic $Cs_4M(II)M(III)_2X_{12}$ layered double perovskites (LDPs), also known as vacancy-ordered quadruple perovskites, have emerged as a promising family of lead-free perovskite materials with superior compositional flexibility.[31–34] As derived from the above-mentioned 3D DP and 2D LP structures, the $Cs_4M(II)M(III)_2X_{12}$ LDPs can be achieved either by using one M(II) and one vacancy to replace two M(I) metal cations of $Cs_2M(I)M(III)X_6$ DP (Scheme 1), or by inserting one additional layer of $M(II)X_6$ octahedra in between the two adjacent layers of $M(III)X_6$ octahedra in 2D $Cs_3M(III)_2X_9$ LPs (Scheme 1). This unique crystal structure with diverse composition selections endows LDPs with characteristic properties, including adjustable band structures and band-gap energies, tunable optical and electronic properties, controllable magnetic orderings, enhanced material and crystal structural stabilities, etc.[35–40]

Ever since the discovery, LDPs have garnered extensive research attention owing to their great promise in technological applications and provoked experimental efforts toward fabrications of various LDPs with diverse metal permutations.[41–48] In 2017, Vargas et al. reported the first example of $Cs_4CuSb_2Cl_{12}$ LDP powder samples, which showed a direct band gap of 1.0 eV with high conductivity and photo/thermal stability.[31] Subsequently, a family of $Cs_4M(II)M(III)_2X_{12}$ LDPs expanded with various combinations of M(II) and M(III) metal cations (M(II): Cu, Mn, Cd, Sn; M(III): Bi, Sb) together with their solid solutions with mixed M(II) or M(III) cations, such as $Cs_4Cd_xMn_{1-x}Bi_2Cl_{12}$, $Cs_4Cu_xMn_{1-x}Sb_2Cl_{12}$, $Cs_4Cd_{0.8}Mn_{0.2}(Sb_xBi_{1-x})_2Cl_{12}$, etc.[36–40,44,49] Within the family, $Cs_4CdSb_2Cl_{12}$ LDPs arguably represent a promising intrinsic p-type transparent conductor.[50–52] The associated high hole conductivity and optical transparency of $Cs_4CdSb_2Cl_{12}$ LDPs stem from a small hole effective mass and a sufficiently large band gap (~3 eV) predicted by first-principles density functional theory (DFT) calculations.[51] Synthesis of bulk $Cs_4CdSb_2Cl_{12}$ LDPs has recently been demonstrated,[42,51] showing their potential to serve as a "warm" white light emitter.[42] Compared with bulk materials, colloidal perovskite NCs with controlled size and morphology offer solution processability and can provide emerging photophysical properties that are inaccessible to bulk materials. However,

[1]Department of Chemistry, Brown University, Providence, RI 02912, USA

[2]Shenzhen Institute of Information Technology, Shenzhen, Guangdong 518172, P.R. China

[3]Center for Nanoscale Materials, Argonne National Laboratory, Lemont, IL 60439, USA

[4]Department of Physics and Astronomy, Ultrafast Photophysics of Quantum Devices Laboratory, Clemson University, Clemson, SC 29634, USA

[5]Center for Functional Nanomaterials, Brookhaven National Laboratory, Upton, NY 11973, USA

[6]Lead contact

*Correspondence: ouchen@brown.edu

https://doi.org/10.1016/j.matt.2021.07.018

despite the synthetic advances in LDPs at bulk scales, synthesis of LDPs in the form of colloidal NCs has been largely limited.[33,35,46,49] Recently, our group reported the first example of colloidal synthesis of $Cs_4CuSb_2Cl_{12}$ LDP NCs,[33] and later extended to a series of Bi-based $Cs_4Cd_{1-x}Mn_xBi_2Cl_{12}$ ($0 \leq x \leq 1$) LDP NCs.[49] However, colloidal synthesis of $Cs_4Cd_{1-x}Cu_xSb_2Cl_{12}$ ($0 \leq x \leq 1$) LDP NCs has not yet been reported, limiting further property exploration and application realization of $Cs_4Cd_{1-x}Cu_xSb_2Cl_{12}$ ($0 \leq x \leq 1$) LDP-based materials when downscaling to a quantum confined nanometer region.

Here, we report a colloidal synthesis of $Cs_4CdSb_2Cl_{12}$ LDP NCs through a hot-injection approach. Detailed optical and structural characterizations showed that the resulting NCs possess a trigonal LDP crystal phase with a direct band-gap energy of 3.19 eV. We further synthesized a series of $Cs_4Cd_{1-x}Cu_xSb_2Cl_{12}$ ($0 \leq x \leq 1$) LDP NCs to provide insights on the composition-structure-property relations of the two types of LDP NCs. We found that the crystal structure of $Cs_4Cd_{1-x}Cu_xSb_2Cl_{12}$ LDP NCs transformed from a trigonal to monoclinic structure when increasing the Cu concentration. Meanwhile, DFT calculations revealed that the magnetism of the $Cs_4Cd_{1-x}Cu_xSb_2Cl_{12}$ ($0 \leq x \leq 1$) LDP NCs evolved from diamagnetic, through ferromagnetic (FM), and finally to antiferromagnetic (AFM) ordering. A band-gap energy reduction to below 2 eV was observed for all the Cu-containing samples, which was due to the introduction of the inter-band electronic state largely contributed from Cu 3d orbital. Calculations for charge distribution and bond characteristics further supported our experimental results on both structural and electronic transformation. Moreover, the transient-absorption (TA) measurements on $Cs_4CdSb_2Cl_{12}$ and $Cs_4Cd_{0.5}Cu_{0.5}Sb_2Cl_{12}$ LDP NCs showed that both types of NCs exhibited ultrafast hot-carrier relaxation dynamics. The introduction of Cu to the NC lattices induces an additional photodynamic channel associated with a mid-gap energy level, which is consistent with our steady-state absorption spectra and band structure calculations. Finally, we demonstrated that the colloidal $Cs_4CdSb_2Cl_{12}$ LDP NCs can be solution processed into high-speed photodetectors with superior performances.

RESULTS AND DISCUSSION

Synthesis and characterizations of $Cs_4CdSb_2Cl_{12}$ LDP NCs

Colloidal $Cs_4CdSb_2Cl_{12}$ LDP NCs were synthesized using a modified hot-injection method with fully decoupled metal cation and halide anion precursors.[23,53–54] In brief, cesium acetate, cadmium acetate, and antimony acetate, with a molar ratio of 2.84:1.00:2.00, were mixed with oleic acid/oleylamine (volume ratio of 4:1) and 1-octadecene. The resulting solution was heated to 120°C under vacuum to remove water and oxygen, then heated to 180°C in a N_2 atmosphere. When the temperature reached 180°C, chlorotrimethylsilane was quickly injected to the solution to initiate NC nucleation and growth. After 15 s, the reaction solution was cooled down to room temperature, and the obtained LDP NCs were purified and dispersed in hexane. Figure 1A shows the absorption profile of the obtained $Cs_4CdSb_2Cl_{12}$ LDP NCs with an absorption onset around 389 nm. The corresponding band gap was determined to be 3.19 eV by a Tauc plot analysis based on a direct allowed transition (Figure 1A, inset).[55] The band gap of LDP NCs is slightly larger than that obtained from DFT calculations and experimental observations for bulk materials, which can be ascribed to the weak quantum confinement.[31,35,41,43,46] No photoluminescence was detected for the $Cs_4CdSb_2Cl_{12}$ LDP NCs at room temperature, likely due to the existence of surface trap states as well as strong exciton-phonon coupling induced fast carrier trapping processes.[23,35,56] Powder X-ray diffraction (XRD) pattern of the $Cs_4CdSb_2Cl_{12}$ LDP NCs (Figure 1B) confirms a trigonal phase with

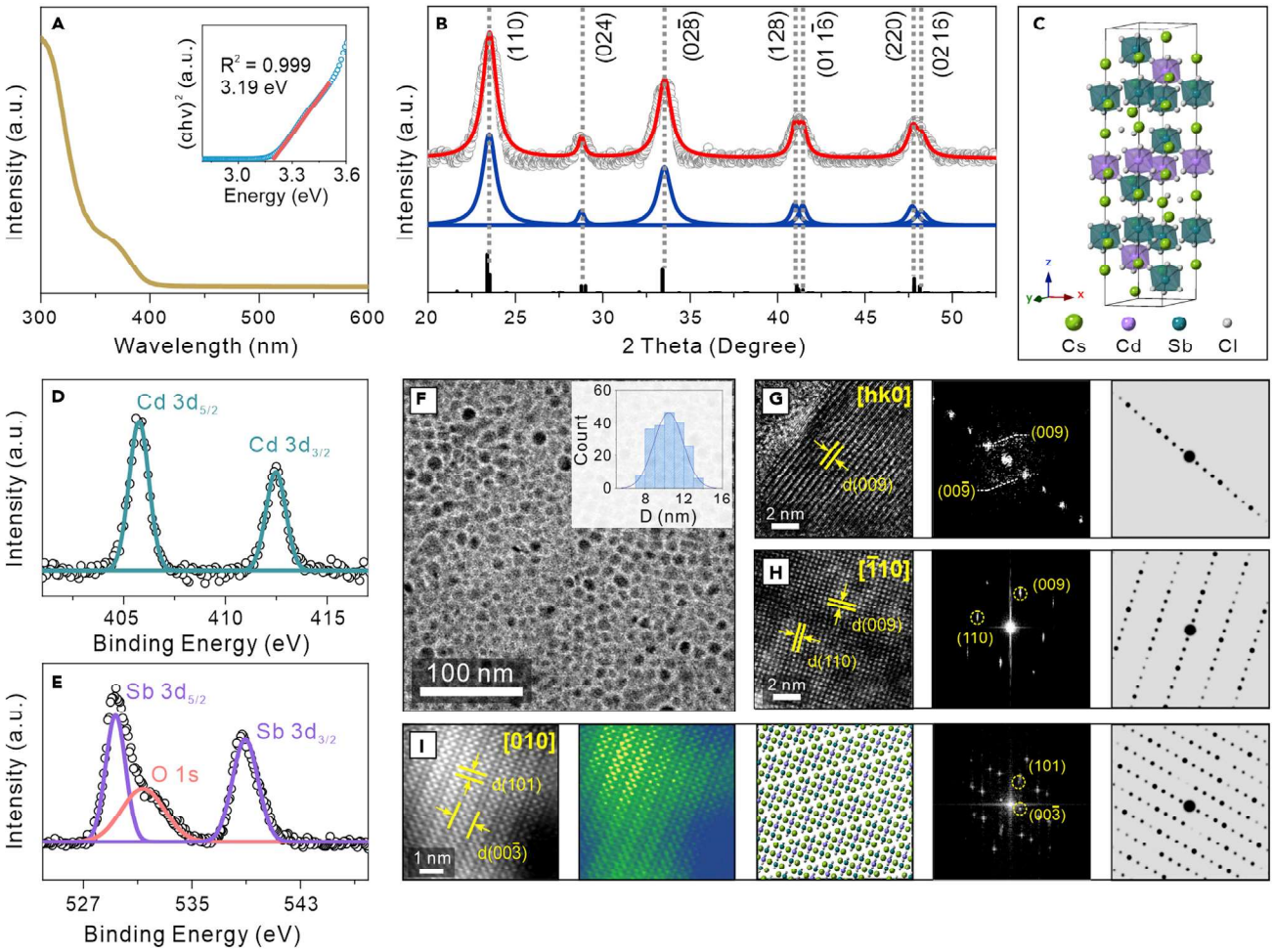

Figure 1. Characterizations of $Cs_4CdSb_2Cl_{12}$ LDP NCs

(A) Absorption spectrum of $Cs_4CdSb_2Cl_{12}$ LDP NCs in hexane. Inset: Tauc plot used to determine the band gap.

(B) XRD pattern (gray line) of the $Cs_4CdSb_2Cl_{12}$ LDP NCs, fitted curve (red line), and constituent peaks (blue line). Black bars indicate the standard peak positions of bulk $Cs_4CdSb_2Cl_{12}$ LDP.[42]

(C) Unit cell of the $Cs_4CdSb_2Cl_{12}$ LDP crystal structure.

(D and E) HR-XPS spectra of the $Cs_4CdSb_2Cl_{12}$ LDP NCs confirming the existence of Cd^{2+} (D) and Sb^{3+} (E) ions. The spectra were calibrated using the C 1s peak.

(F) Low-magnification TEM image. Inset: particle diameter (D) distribution histogram of the LDP NCs.

(G and H) HR-TEM images of $Cs_4CdSb_2Cl_{12}$ LDP NCs (left panels), the corresponding fast-Fourier transformation (FFT) patterns (middle panels), and computer-simulated electron diffraction (ED) patterns (right panels) along the [hk0] (G) ([−10 1 0] was used for simulation) and [$\bar{1}$10] (H) directions of the LDP crystal structure.

(I) The panels from left to right are the representative HAADF-STEM image of $Cs_4CdSb_2Cl_{12}$ LDP NCs along the [010] zone axis, the corresponding Pseudocolor image, computer-simulated 3D atomic model (green, Cs; purple, Cd; blue, Sb; gray, Cl), the associated FFT pattern, and the simulated ED pattern.

the vacancy-ordered LDP crystal structure (space group: $R\bar{3}m$; Figure 1C; Table S1). The positions of all the Bragg diffraction peaks matched well with the simulated standard peak positions of the bulk $Cs_4CdSb_2Cl_{12}$ LDP.[42] The broadening effects for diffraction peaks were consistent with the finite crystalline sizes (Figure 1B).[31,57] The lattice parameters were determined to be $a = 7.602$ Å and $c = 36.90$ Å (Figure 1B; Table S1). High-resolution (HR) X-ray photoelectron spectroscopy (XPS) measurements prove the composition and valence states of Cd^{2+} and Sb^{3+} ion centers in the $Cs_4CdSb_2Cl_{12}$ LDP NCs (Figures 1D, 1E, and S1). Scanning electron microscopy energy-dispersive X-ray spectroscopy (SEM-EDS) analysis specified the atomic ratio

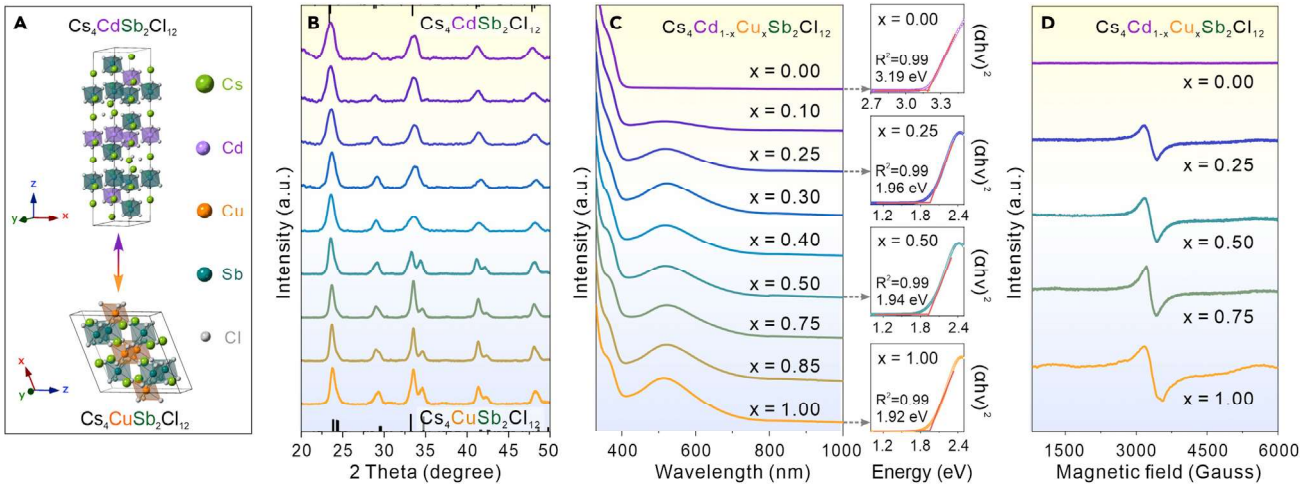

Figure 2. Phase transformation of $Cs_4Cd_{1-x}Cu_xSb_2Cl_{12}$ LDP NCs

(A) Scheme of the atomic models for the structural transformation from $Cs_4CdSb_2Cl_{12}$ LDP in the trigonal phase (top) to $Cs_4CuSb_2Cl_{12}$ LDP in the monoclinic phase (bottom).

(B) XRD patterns of $Cs_4Cd_{1-x}Cu_xSb_2Cl_{12}$ LDP NCs (from top to bottom: x = 0.00, 0.10, 0.25, 0.30, 0.40, 0.50, 0.75, 0.85, and 1.00).

(C) Absorption spectral evolution of the $Cs_4Cd_{1-x}Cu_xSb_2Cl_{12}$ LDP NCs (left panel) and four selected Tauc plots to determine the band-gap energy (right panels).

(D) EPR spectra of $Cs_4Cd_{1-x}Cu_xSb_2Cl_{12}$ LDP NCs (from top to bottom: x = 0.00, 0.25, 0.50, 0.75, and 1.00).

of Cs:Cd:Sb:Cl as 3.61:1.00:1.78:11.59 (Figure S2), which was close to the stoichiometry of $Cs_4CdSb_2Cl_{12}$ NCs. Transmission electron microscopy (TEM) image manifested that the $Cs_4CdSb_2Cl_{12}$ LDP NCs possessed a spherical-like shape with an average diameter of 10.4 $\pm$ 1.5 nm (Figure 1F). HR-TEM images exhibited clear lattice fringes (left panels in Figures 1G and 1H), indicating high crystallinity of the $Cs_4CdSb_2Cl_{12}$ LDP NCs. For example, the observed d-spacings of 4.0 and 3.9 Å in Figure 1H, can be assigned to the (009) and (110) crystal planes, respectively, projected from the viewing direction of [$\bar{1}$10]. The corresponding fast-Fourier transformation patterns together with the computer-simulated electron diffraction patterns confirmed the lattice plane and projection assignments (Figures 1G and 1H). High-angle annular dark-field scanning TEM (HAADF-STEM) measurements were also performed to provide insights of the LDP crystal structure of the $Cs_4CdSb_2Cl_{12}$ NCs with atomic precision (Figure 1I). Figure 1I shows clear periodic lattices with a lamellar-type atomic arrangement. The measured lattice d-spacings of 12.1 and 6.2 Å were, respectively, assigned to the (00$\bar{3}$) and (101) crystal planes along the [010] zone axis of the trigonal LDP crystal structure. The cross-fringes in this projection exhibit an angle of 97.2°, which is in good agreement with the theoretical value of 100.1°. In addition, negligible changes were observed for the absorption spectra and XRD patterns of the $Cs_4CdSb_2Cl_{12}$ LDP NCs after storing for at least 8 weeks, indicating their good stability under ambient conditions (Figure S3). Taken together, these results unambiguously confirmed the successful synthesis of stable colloidal $Cs_4CdSb_2Cl_{12}$ LDP NCs.

Transformation of $Cs_4Cd_{1-x}Cu_xSb_2Cl_{12}$ ($0 \leq x \leq 1$) LDP NCs

Composition tuning has been explored in perovskite NCs due to their rich polymorphs and associated influences on the induced crystal and electronic structure transformation. In particular, the combination of Cd-Cu composition with inter-LDP-NC transformation has not yet been reported. To build the composition-structure-property relationship of the LDP NCs, a series of $Cs_4Cd_{1-x}Cu_xSb_2Cl_{12}$ ($0 \leq x \leq 1$) NCs were synthesized by changing the molar ratio of Cd^{2+} and Cu^{2+}

precursors (Figure 2A; also see experimental procedures for details). HR-XPS spectra confirmed the co-existence of Cd^{2+} and Cu^{2+} in the $Cs_4Cd_{1-x}Cu_xSb_2Cl_{12}$ LDP NCs ($0 < x < 1$), where the 3d signals ($3d_{5/2}$ and $3d_{3/2}$) of Cd^{2+} and 2p signals ($2p_{3/2}$ and $2p_{1/2}$) of Cu^{2+} could both be observed (Figure S4). In contrast, no Cu^{2+} (Cd^{2+}) signals in the XPS spectra were detected for $Cs_4CdSb_2Cl_{12}$ ($Cs_4CuSb_2Cl_{12}$) LDP NCs (Figure S4). Consistently, the inductively coupled plasma-atomic emission spectroscopy (ICP-AES) measurements revealed the stoichiometric ratio of ([Cu]+[Cd])/[Sb] was ~0.5, with the [Cu]/([Cu]+[Cd]) ratio matching well with the precursor feeding ratio (Table S2). TEM images show similar particle size, shape, and size distribution for the $Cs_4Cd_{1-x}Cu_xSb_2Cl_{12}$ ($0 \leq x \leq 1$) NCs (Figures 1F and S5), indicating a minimal morphological influence made by replacing Cd^{2+} with Cu^{2+} of these LDP NCs. The XRD patterns showed that the trigonal LDP crystal structure was preserved for the $Cs_4Cd_{1-x}Cu_xSb_2Cl_{12}$ LDP NCs with x ranging from 0.00 to 0.40 (Figure 2B). Meanwhile, all the diffraction peaks shifted to higher angles monotonically, revealing a lattice contraction with the increased Cu^{2+} concentration (Figures 1B and S6–S9; Tables S1 and S3–S6), in agreement with the replacement of Cd^{2+} cations (ionic radius: 109 pm) by smaller Cu^{2+} (ionic radius: 73 pm) cations. With the increased Cu^{2+} content ($x \geq 0.5$), the crystal phase transitioned from the original trigonal to the final monoclinic LDP structure of the $Cs_4CuSb_2Cl_{12}$ LDP NCs (Figures 2A and S10–S13; Tables S7–S10).[31,33] This crystal phase transition process was demonstrated by the broadening of the $(02\bar{8})$ diffraction peak (~33.6°) of the trigonal phase and eventual splitting into two distinct $(40\bar{4})$ and (222) peaks of the monoclinic phase (Figures 2B and S10–S13; Tables S7–S10). UV-vis absorption spectral evolution was also monitored for the $Cs_4Cd_{1-x}Cu_xSb_2Cl_{12}$ LDP NCs ($0 \leq x \leq 1$) (Figure 2C). The results showed that, after Cu^{2+} incorporation, a broad absorption peak emerged at around 515 nm, which is consistent with the introduction of inter-band-gap electronic state by the Cu component (also supported by the DFT calculation discussed below).[31,33] With the increased Cu^{2+} concentration, this newly emerged absorption band increased in intensity. Tauc plot analyses quantified that the band-gap energy exhibited a gradual redshift from 1.97 to 1.92 eV when increasing x from 0.10 to 1.00 (Figures 2C and S14). Along with the emergence of the new absorption feature, an electron paramagnetic resonance (EPR) peak centered at 3,314 G (g factor: 2.076) appeared upon introducing Cu component (Figure 2D), in accordance with the presence of unpaired electron of Cu^{2+} ions (electron configuration: $[Ar]3d^9$). The increased asymmetricity of the EPR peak was due to the increased Jahn-Teller distortion of $[CuCl_6]^{4-}$ octahedra in the LDP crystal structure, which was confirmed by the DFT calculation discussed in the next session.[41,58–61]

DFT calculations

To shed more light on the evolutions of crystal structure, magnetic ordering, and the corresponding electronic band structure induced by the composition tuning, we performed DFT calculations on $Cs_4Cd_{1-x}Cu_xSb_2Cl_{12}$ ($0 \leq x \leq 1$) LDPs using generalized gradient approximation formulated by the Perdew-Burke-Ernzerhof (PBE) functional using Vienna *ab initio* Simulation Package (VASP) software (Figure 3; see computational methods for the calculation details).[31,39,62–64] The stable crystal structures were determined by calculating the total energy of $Cs_4Cd_{1-x}Cu_xSb_2Cl_{12}$ ($0 \leq x \leq 1$) LDPs with consideration of preferred magnetic orderings (Figures S15–S17). Figures 3E and S17 show that $Cs_4Cd_{1-x}Cu_xSb_2Cl_{12}$ LDPs in the trigonal phase exhibit a diamagnetic ordering when x = 0.00, while they exhibit a FM ordering when x = 0.25 and 0.33. When x increased to 0.50 and higher (i.e., x = 0.50, 0.75, and 1), the monoclinic phase with an AFM ordering becomes the thermodynamically preferred crystal structure for the $Cs_4Cd_{1-x}Cu_xSb_2Cl_{12}$ LDPs (Figures 3E

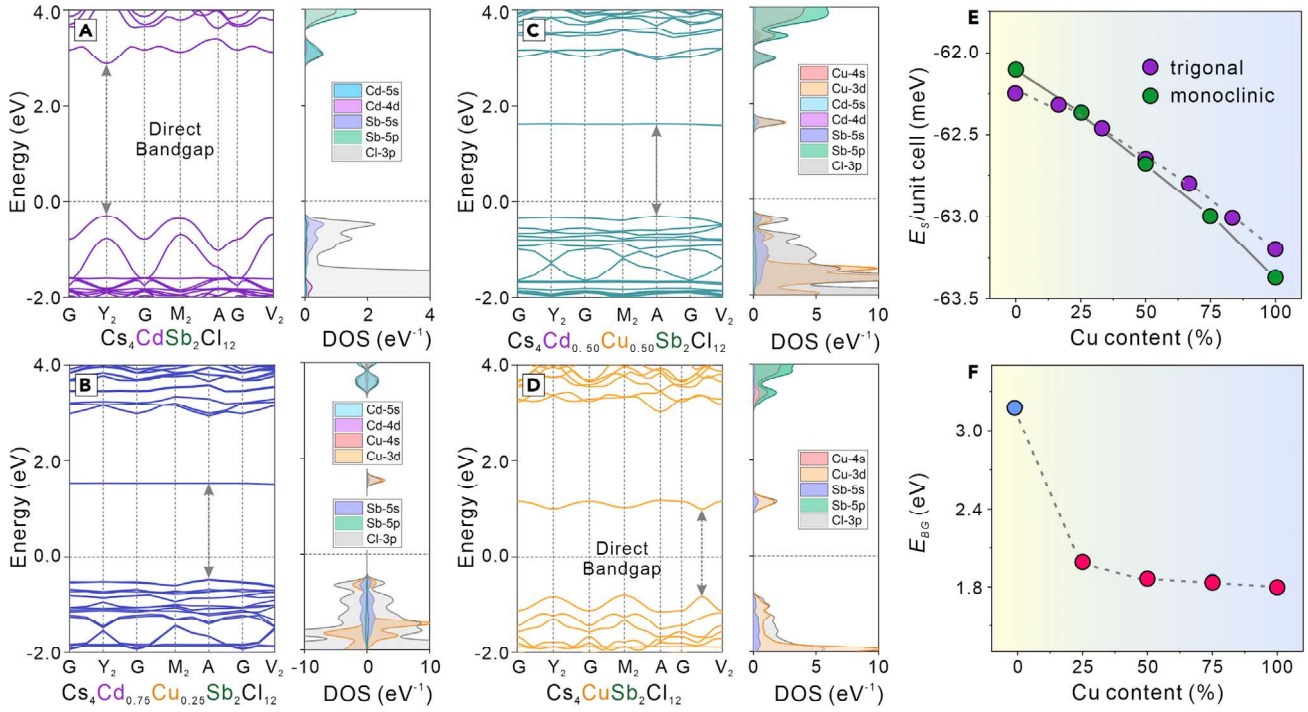

Figure 3. Band structure and density of state calculations of $Cs_4Cd_{1-x}Cu_xSb_2Cl_{12}$ LDPs

(A–D) Calculated band structures (left panels) and the corresponding projected density of state (DOS) diagrams (right panels) of the $Cs_4Cd_{1-x}Cu_xSb_2Cl_{12}$ LDPs with x = 0 (A), x = 0.25 (B), x = 0.50 (C), and x = 1.00 (D). Horizontal gray dashed lines represent the Fermi energy level.

(E) Total energy of $Cs_4Cd_{1-x}Cu_xSb_2Cl_{12}$ ($0 \leq x \leq 1$) LDPs per unit cell in the trigonal and monoclinic phases.

(F) The corresponding calculated band-gap energies (E_{BG}) of $Cs_4Cd_{1-x}Cu_xSb_2Cl_{12}$ ($0 \leq x \leq 1$) LDPs with different Cu content.

and S17). These calculation results are in accordance with the experimental observation (Figure 2B).

Upon determining the stable crystal phases, the electronic structures of $Cs_4Cd_{1-x}Cu_xSb_2Cl_{12}$ (x = 0.00, 0.25, 0.50, 0.75, and 1.00) LDPs were further investigated, and the results are shown in Figures 3A–3D and S18. In the case of $Cs_4CdSb_2Cl_{12}$ in trigonal phase, a direct band gap of 3.18 eV with both conduction band minimum (CBM) and valence band maximum (VBM) located at the Y_2 symmetry point was calculated (Figure 3A, left panel). The corresponding projected density of state (DOS) calculations show that the CBM is mostly contributed by Sb 5p, Cl 3p, and Cd 5s orbitals, while the VBM is mainly composed of Cl 3p and Sb 5s orbitals (Figure 3A, right panel). For the intermediate $Cs_4Cd_{1-x}Cu_xSb_2Cl_{12}$ (x = 0.25, 0.50, and 0.75) LDPs, the calculation results are shown in Figures 3B, 3C, and S18. While the $Cs_4Cd_{0.75}Cu_{0.25}Sb_2Cl_{12}$ is stable in trigonal phase, its band structure is closer to the $Cs_4CuSb_2Cl_{12}$ with a decreased band-gap energy of 1.99 eV (Figures 3B and 3F). The sharp decrease of band-gap energy can be attributed to the introduction of new CBM contributed by Cu 3d and Cl 3p orbitals with a small portion of Sb 5s orbitals (Figure 3B). The DOS shows unequal spin-up and spin-down states around the Fermi level, resulting in the FM characteristic. When Cu content is further increased to x = 0.50 and 0.75, their band structures preserve a direct band-gap feature with the band-gap energy narrowing to 1.88 and 1.86 eV, respectively, matching well with the Tauc plot analysis for the corresponding absorption spectra (Figures 2C and S14). The contribution of the Cu 3d orbital to the CBM is larger with the increased Cu content, while the VBM remains mainly composed of Cu 3d, Cl 3p, and Sb 5s orbitals. In the case of $Cs_4CuSb_2Cl_{12}$ LDP, theoretical calculations

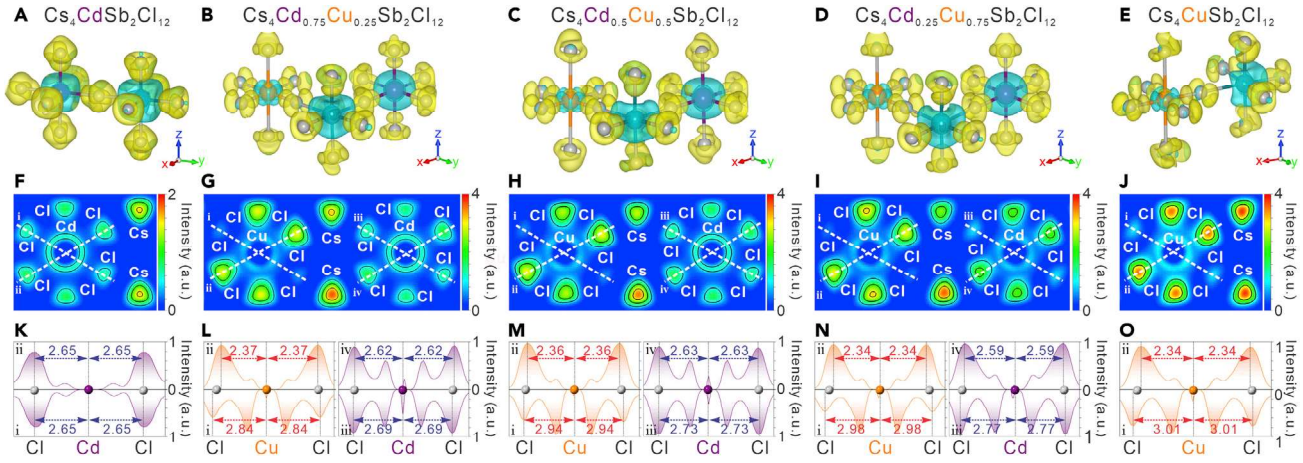

Figure 4. Charge density difference and electron localization function of $Cs_4Cd_{1-x}Cu_xSb_2Cl_{12}$ LDPs

(A–E) Charge density difference of $Cs_4Cd_{1-x}Cu_xSb_2Cl_{12}$ LDPs with $x = 0.00$ (A), $x = 0.25$ (B), $x = 0.50$ (C), $x = 0.75$ (D), and $x = 1.00$ (E). In (A)–(E), yellow and blue surfaces mean the charge gain and charge loss, respectively.

(F–J) Electron localization function (ELF) of $Cs_4Cd_{1-x}Cu_xSb_2Cl_{12}$ LDPs with $x = 0.00$ (F), $x = 0.25$ (G), $x = 0.50$ (H), $x = 0.75$ (I), and $x = 1.00$ (J). In (F)–(J), the colors in ELF 2D mapping indicate the strength of electron density.

(K–O) 1D intensity profiles of $Cs_4Cd_{1-x}Cu_xSb_2Cl_{12}$ LDPs with $x = 0.00$ (K), $x = 0.25$ (L), $x = 0.50$ (M), $x = 0.75$ (N), and $x = 1.00$ (O) along two white dashed lines in the corresponding ELF 2D mapping in (F–J), demonstrating the evolution of electron density changes between Cd^{2+}/Cu^{2+} and Cl^- ions for clear visualization of gradual distortions of $[CdCl_6]^{4-}$ and $[CuCl_6]^{4-}$ octahedral units in the $Cs_4Cd_{1-x}Cu_xSb_2Cl_{12}$ LDPs.

revealed an intra-layer AFM ordering with a direct band gap of 1.81 eV, with both VBM and CBM located at the same symmetry point in between G and V_2 (Figure 3D).[33] While both CBM and VBM are dominated by Cu 3d and Cl 3p orbitals with a little contribution from Sb 5s orbital. The summary of calculated band-gap energies (E_{BG}) is shown in Figure 3F. A sudden decrease in band-gap energy after incorporating Cu into LDPs indicates the effects of Cu contribution on the band structures, matching well with the experimental results for the evolution of absorption spectra (Figures 2C and S14).

To gain further insights of the charge distribution and bond features of $Cs_4Cd_{1-x}Cu_xSb_2Cl_{12}$ LDPs during the transformation, the charge density difference and electron localization function (ELF) were calculated and shown in Figure 4 (see details in the experimental procedures). In the case of $Cs_4CdSb_2Cl_{12}$ LDPs (i.e., $x = 0$), no apparent charge redistribution was found due to equal electron donation from Cd^{2+} to Cl^- ions in perfect $[CdCl_6]^{4-}$ octahedra (Figure 4A). The associated 2D ELF mapping illustrates an ionic bond nature of Cd–Cl bonds supported by the minimal electron density between Cd^{2+} cations and Cl^- anions (Figure 4F). The corresponding 1D intensity profiles along the white dashed lines further prove the identical Cd–Cl bond length of a perfect $[CdCl_6]^{4-}$ octahedron (Figure 4K). With the increased Cu^{2+} concentration ($x = 0.25$, 0.50, and 0.75), a gradual elongation along the z direction in the $[CuCl_6]^{4-}$ octahedra was observed (the Cu–Cl bond length changed from 2.84 to 2.98 Å along the *z* direction), indicating the enhanced Cu-induced Jahn-Teller effect (with singly occupied degenerated e_g molecular orbitals) (Figures 4B–4D and S19 and Table S11).[33,59] The 2D ELF mapping consistently shows a decreased electron density, thus weaker Cu–Cl bonds along the *z* direction in comparison with those in the *x*-*y* plane (Figures 4G–4I). Meanwhile, the neighboring $[CdCl_6]^{4-}$ and $[SbCl_6]^{3-}$ octahedra consequently became distorted after Cu^{2+} introduction (Tables S12 and S13). This increased distortion can be ascribed to the synergic effects of adjacent twisted $[CuCl_6]^{4-}$ due to their interconnection nature. The 1D electron density profiles for different octahedral units

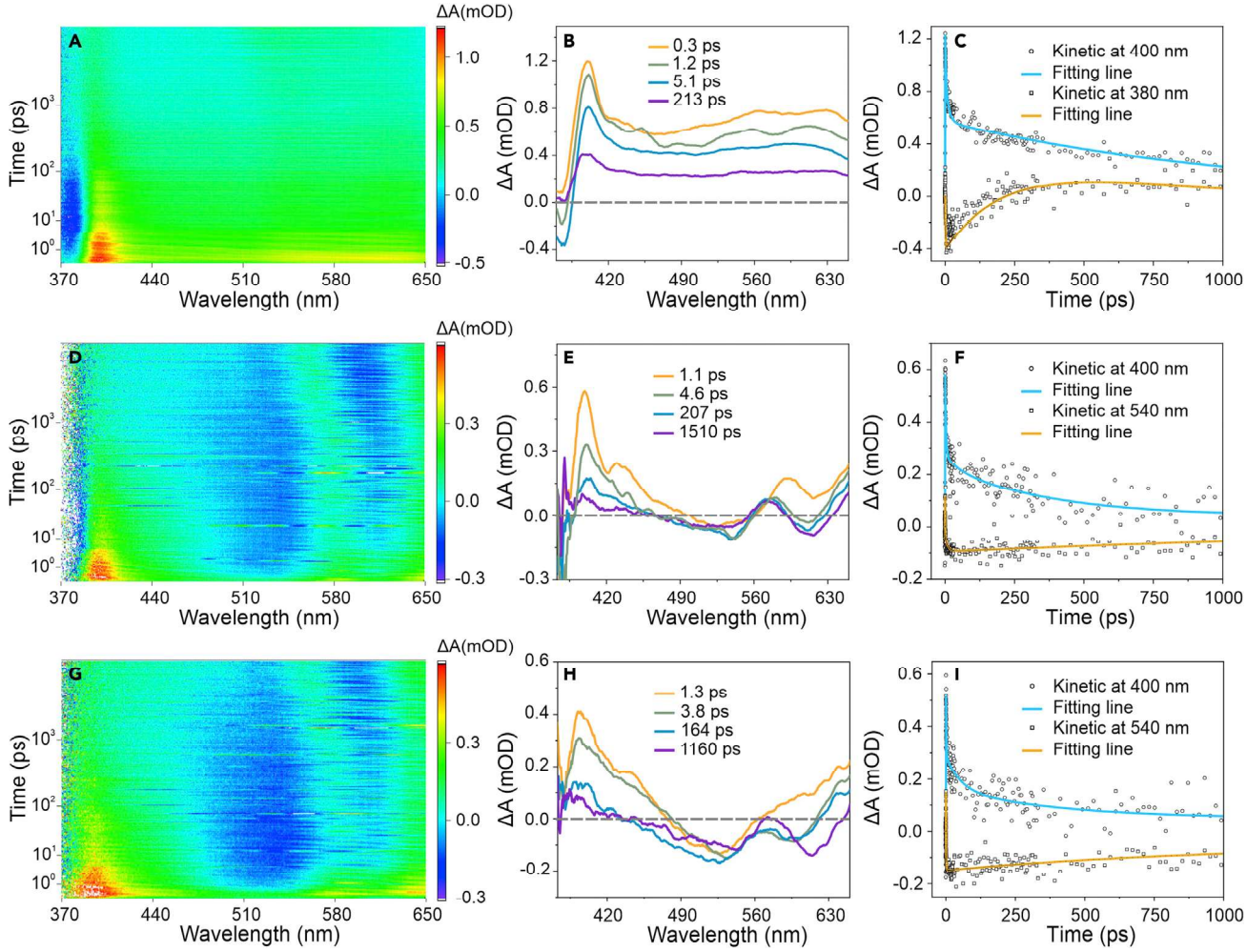

Figure 5. Transient-absorption measurements of $Cs_4Cd_{1-x}Cu_xSb_2Cl_{12}$ (x = 0.00, 0.50, and 1.00) LDP NCs

(A–C) Pseudocolor transient-absorption (TA) plots (A), TA spectra at the varied delay time (B), and PIA and GSB decay dynamics (C) for $Cs_4CdSb_2Cl_{12}$ LDP NCs.

(D–F) Pseudocolor TA plots (D), TA spectra at the varied delay time (E), and PIA and GSB decay dynamics (F) for $Cs_4Cd_{0.5}Cu_{0.5}Sb_2Cl_{12}$ LDP NCs.

(G–I) Pseudocolor TA plots (G), TA spectra at the varied delay time (H), and PIA and GSB decay dynamics (I) for $Cs_4CuSb_2Cl_{12}$ LDP NCs.

(i.e., $[CuCl_6]^{4-}$ and $[CdCl_6]^{4-}$, Figures 4L–4N) unambiguously elucidate their gradual distortions during the compositional evolution. Finally, when reaching the $Cs_4CuSb_2Cl_{12}$ LDP, the large $[CuCl_6]^{4-}$ octahedral distortion resulted in a net charge loss along the Cu–Cl bonds in the *x*-*y* plane with no obvious changes observed in the *z* direction (blue surfaces, Figure 4E). Consistently, the 2D ELF mapping and 1D electron density profiles demonstrated the elongated Cu–Cl bonds (bond length of 3.01 Å) along the *z* direction and the shortened ones (bond length of 2.34 Å) in the equatorial *x* and *y* directions (Figures 4J and 4O; Table S11).

TA spectroscopy

To understand the charge carrier dynamics of the LDP NCs, femtosecond TA was employed to study and compare the differences between $Cs_4CdSb_2Cl_{12}$ and $Cs_4Cd_{0.5}Cu_{0.5}Sb_2Cl_{12}$ LDP NCs. Figure 5A shows the Pseudocolor TA plot of $Cs_4CdSb_2Cl_{12}$ LDP NCs, which possesses a ground state bleach (GSB) signal at around 380 nm together with a broad photo-induced absorption (PIA) band on the red side from 390 to 420 nm. This GSB signal paired with the PIA signal at longer

wavelengths has been observed in other perovskite NCs and can be attributed to strong interactions of excitons at the red side of band edge transition (Figure 5B).[23,56,65] It can be seen from Figure 5C that the buildup of the PIA signal is accompanied by the decay of the GSB feature, indicating that the dynamics of the PIA band is related to carrier intra-band relaxation.[23,65,66] Interestingly, the $Cs_4Cd_{0.5}Cu_{0.5}Sb_2Cl_{12}$ LDP NCs exhibit strikingly distinct photodynamics compared with the $Cs_4CdSb_2Cl_{12}$ LDP NCs (Figures 5D–5F). A PIA signal associated with strong exciton-exciton interactions was detected from 390 to 420 nm, which is similar to the case of $Cs_4CdSb_2Cl_{12}$ LDP NCs. However, two additional GSB signals are found at the longer wavelength side from 480 to 550 nm and from 580 to 620 nm (Figures 5D and 5E). These bleaching signals, which are not observed in the $Cs_4CdSb_2Cl_{12}$ LDP NCs, are likely due to sub-band-gap absorption induced by the Cu substitutions, consistent with the inter-band level introduced by Cu shown in the band structures of the $Cs_4Cd_{0.5}Cu_{0.5}Sb_2Cl_{12}$ LDP NCs (Figure 3C). It also matches well with the new absorption peak in the steady-state absorption spectra in Figure 2C after the introduction of Cu into the $Cs_4CdSb_2Cl_{12}$ LDP. In addition, the GSB signals around 380 nm are missing/much weaker for $Cs_4Cd_{0.5}Cu_{0.5}Sb_2Cl_{12}$ LDP NCs compared with those of $Cs_4CdSb_2Cl_{12}$ LDP NCs, while the decay of the PIA signal at 400 nm is associated with the rise of the GSB signal at 540 nm (Figure 5F). These are also likely caused by bleaching of the PIA signal at 400 nm to the mid-gap level related to Cu incorporation. Consistently, the $Cs_4CuSb_2Cl_{12}$ LDP NCs behaved similarly to the $Cs_4Cd_{0.5}Cu_{0.5}Sb_2Cl_{12}$ LDP NCs in the TA measurements (Figures 5G–5I). Taken together, for the $Cs_4CdSb_2Cl_{12}$ LDP NCs, the PIA peak at 400 nm is mainly associated with the rising of the bleaching band at 380 nm caused by exciton-exciton interactions. However, when Cu is introduced to the NCs, the 400 nm band is instead associated with the bleaching signal at 540 nm, where the mid-gap level is introduced by Cu incorporation. This result demonstrates that the carrier relaxation from band edge to the mid-gap level beats their transition into the high-energy levels at 380 nm.

Ultrafast photodetector

Based on the DFT calculations and TA studies, $Cs_4CdSb_2Cl_{12}$ LDP NCs possess surpassing charge transport characteristics and unique carrier dynamics,[51] which can be further characterized by ultrafast photocurrent spectroscopy. The detailed device fabrication and experimental configurations can be found in the experimental procedures (Figures 6A and S20). In brief, the thin-film LDP photoconductive device was constructed by drop-casting concentrated $Cs_4CdSb_2Cl_{12}$ LDP NC solution (20 mg/mL) on a glass substrate and then integrated into a microstrip transmission line structure. Upon ultrafast laser illumination, photogenerated charge carriers were collected as a photocurrent *in situ* by a sampling oscilloscope. As is shown in Figure 6B, the measured ultrafast photocurrent peak intensity is over three orders of magnitude higher than the dark photocurrent, supporting its superior charge transport characteristics under light irradiation. In addition, the dependence of applied electrical field, laser intensity, and temperature on the photocurrent are investigated (Figures 6C–6E). The photocurrent spectra show a quick rise time of ~25 ps and an average lifetime of ~150 ps (Figures 6C–6E), highlighting the narrow bandwidth for the high-speed photodetectors. These results indicate a faster time response for the $Cs_4CdSb_2Cl_{12}$ LDP NC-based photodetector compared with the $Cs_4CuSb_2Cl_{12}$ LDP NC-based one (with an extended lifetime of >200 ps).[33] The initial linear dependence of peak photocurrent on the electric field (bias voltage) (Figure 6C, inset) shows the ohmic behavior of the device, similar to the photocurrent behaviors at lower electric fields seen for the $Cs_4CuSb_2Cl_{12}$ NC-based devices.[33] This is confirmed through the dark and light current-voltage (IV) curves in

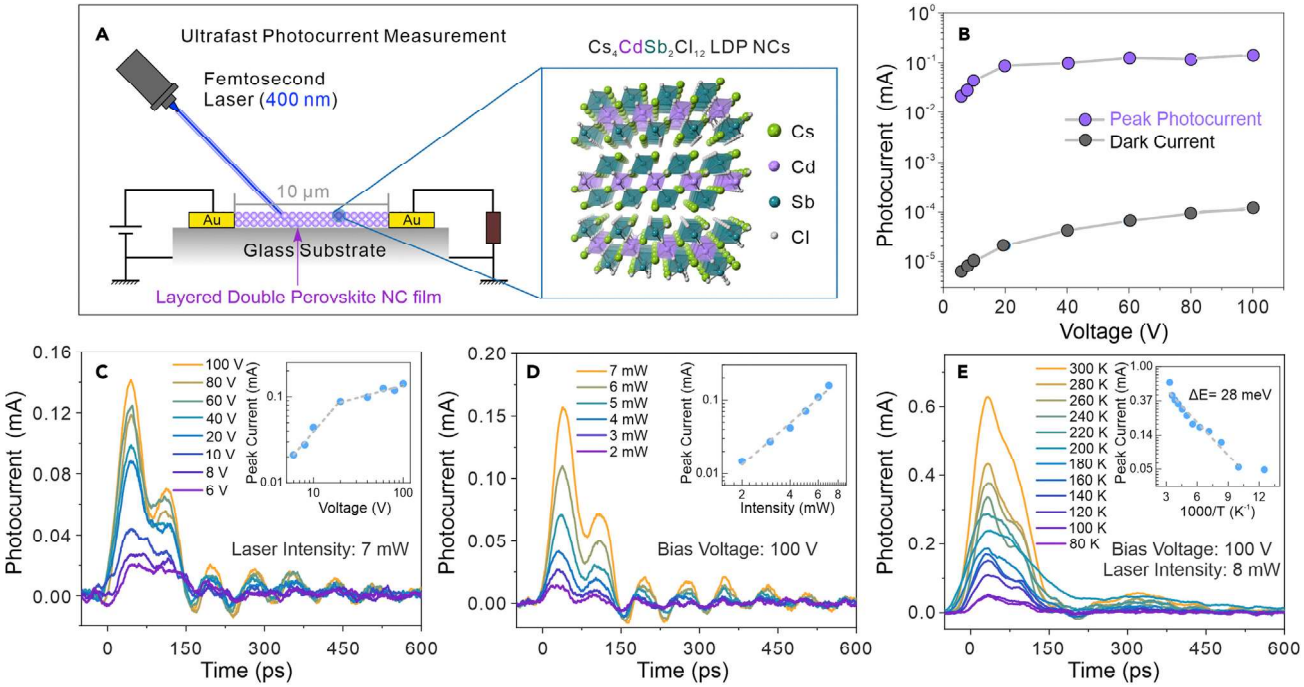

Figure 6. Fabrication and characterizations of ultrafast photodetector

(A) A schematic showing a $Cs_4CdSb_2Cl_{12}$ LDP NC-based high-speed photodetector. The wavelength of ultrafast laser pulse is 400 nm with a duration of 100 fs.

(B) Peak photocurrent and dark current as a function of bias voltage applied to the device measured under illumination and in the dark.

(C–E) Ultrafast photocurrent dependences on the bias voltage (C), laser intensity (D), and temperature (E). Note that the oscillations are due to the impedance mismatch, which are not related to the internal photophysics.

Figure 6B as well. The saturation of the current can be attributed to ionic transport in the higher electric fields (voltages), which may impede the carrier mobility. Figure 6D shows a positive linear relationship of photocurrent as increasing incident light intensity, indicating more photo carriers being generated. The temperature-dependent photocurrent spectra, as shown in Figure 6E, provide insights on the carrier transport mechanism. Upon ultrafast laser excitation, the photogenerated carriers may thermalize to the band edge in the sub-ps timescale, followed by falling into defect states or tunneling to nearby NCs. It can be seen that the photocurrent peak increases with the increased temperature, indicating a trap-assisted transport process.

The energy level of the trap states can be identified by an Arrhenius relation ($e^{-\frac{\Delta E}{k_B T}}$), where k_B is the Boltzmann constant and ΔE is the average activation energy, as shown in the Figure 6E inset. The obtained shallow trap state of ~28 meV further proves that a trap-assisted tunneling process can be responsible for the charge transport mechanism.

Conclusions

In conclusion, we present a new colloidal synthesis of $Cs_4CdSb_2Cl_{12}$ LDP NCs with a wide band gap around 3.19 eV in the trigonal phase. A series of $Cs_4Cd_{1-x}Cu_xSb_2Cl_{12}$ ($0 \leq x \leq 1$) LDP NCs were further studied in experiments and by DFT calculations, demonstrating the composition-structure-properties relations. Phase transformation from trigonal phase to monoclinic phase was found together with the corresponding changes in electronic band structures and magnetic ordering with the increased Cu concentration in the $Cs_4Cd_{1-x}Cu_xSb_2Cl_{12}$ LDP NCs. In addition, deep insights into the charge carrier dynamics are provided based on the

femtosecond TA spectroscopic studies as well as the theoretical calculations of the charge distribution and bond characteristics. Furthermore, we have solution processed $Cs_4CdSb_2Cl_{12}$ LDP NCs into a high-speed photodetector with superior photo-response, demonstrating high potentials of the material for optoelectronic applications. We anticipate that our study can lay out a roadmap for both fundamental studies and practical applications of various lead-free perovskite nanomaterials taking advantages of their unique property characteristics in the future.

EXPERIMENTAL PROCEDURES

Resource availability

Lead contact

Further information and requests for additional details should be directed to and will be fulfilled by the lead contact, Ou Chen (ouchen@brown.edu).

Materials availability

The materials generated in this study will be made available on request.

Data and code availability

All data in the manuscript and supplemental information are available from the lead contact on request.

Materials

Cesium acetate (CsOAc, 99.99%), cadmium acetate dihydrate ($Cd(OAc)_2 \cdot 2H_2O$, 99.999%), copper(II) acetate ($Cu(OAc)_2$, 99.99%), antimony acetate ($Sb(OAc)_3$, 99.99%), oleic acid (OA, technical grade, 90%), oleylamine (OAm, technical grade, 70%), 1-octadecene (ODE, technical grade, 90%), chlorotrimethylsilane (TMS-Cl, ≥99%) and nitric acid (70%, ≥99.999%, trace metals basis) were purchased from Sigma-Aldrich. Hexane and ethyl acetate were purchased from Fisher Scientific. All chemicals were used as received without further purification.

Synthesis of $Cs_4CdSb_2Cl_{12}$ LDP NCs

Colloidal synthesis of $Cs_4CdSb_2Cl_{12}$ LDP NCs was based on a hot-injection method modified by previous reports.[33] CsOAc (68.1 mg, 0.355 mmol), $Cd(OAc)_2 \cdot 2H_2O$ (33.3 mg, 0.125 mmol), and $Sb(OAc)_3$ (74.7 mg, 0.250 mmol) were added into the mixture of OA (1.25 mL), OAm (0.31 mL), and ODE (5.00 mL) in a 50 mL three-neck flask. The mixture was heated to 120°C for 1 h under vacuum to remove water and oxygen. After all precursors were dissolved, the flask was heated to 180°C in a N_2 atmosphere. Upon reaching 180°C, the mixture of 0.25 mL TMS-Cl mixed with 0.25 mL ODE was injected into the solution to initiate the NC nucleation and growth. The solution turned into a turbid white solution immediately. After 15 s, the solution was cooled down using an ice bath. The NCs were purified from ODE in two steps: (1) 20 mL of ethyl acetate was added and then centrifuged at 7,000 rpm (RCF: 5,708) for 10 min. The supernatant was discarded, and the resulting precipitate was dispersed in 10 mL hexane. (2) The solution was centrifuged again at 4,500 rpm (RCF: 2,359) for 5 min and the clear supernatant was collected for further characterization.

Synthesis of $Cs_4Cd_{1-x}Cu_xSb_2Cl_{12}$ ($0 \leq x \leq 1$) LDP NCs

Similar to the synthesis of $Cs_4CdSb_2Cl_{12}$ LDP NCs, a series of $Cs_4Cd_{1-x}Cu_xSb_2Cl_{12}$ ($0 \leq x \leq 1$) LDP NCs were synthesized using a hot-injection method. The NCs with different Cd and Cu concentrations can be obtained by tuning the ratio of precursor amounts while keeping the total amount of Cd and Cu precursors as 0.125 mmol. Other reaction procedures and purification processes were kept the same as the protocol for the synthesis of $Cs_4CdSb_2Cl_{12}$ LDP NCs.

Measurements and characterization

Absorption spectra were measured using an Agilent Technologies Cary 5000 UV-Vis-NIR Spectrophotometer using NC hexane solution samples. Powder XRD patterns were obtained on a Bruker D8 DISCOVER 2D X-ray Diffractometer equipped with a VANTEC 500 2D area detector operating with Cu Kα (λ = 1.541 Å) radiation. XPS spectra were performed on a Thermo Scientific K-Alpha instrument operating on Al Kα = 1,486.6 eV radiation with a spot size of ~200 μm. TEM and high-resolution TEM characterizations were performed on a JEOL 2100F operated at 200 kV. HAADF-STEM images were acquired with Hitachi HD 2700C dedicated STEM with a probe Cs corrector operating at 200 kV. SEM-EDS measurements were performed on a LEO 1530 SEM. ICP-AES measurements were carried out on a Thermo Scientific iCAP 7400 DUO ICP-AES equipped with a Teledyne ASX-560 240 position autosampler. X-band EPR spectra were measured using a Bruker EMX Premium-X EPR Spectrometer using NC hexane solution samples.

Ultrafast TA studies

Ultrafast TA spectra and kinetics were carried out using an amplified Ti:sapphire laser system (Spectra Physics, Spitfire-Pro) and automated data acquisition system (Ultrafast Systems, Helios) using NC hexane solution samples. The amplifier produced 120 fs pulses at 5 kHz. The output from the amplifier was split 90/10 to pump an optical parametric amplifier (Light Conversion, TOPAS). The TA system enables 3D data collection (spectra/time/ΔOD).

The continuum probe beam was generated by first sending the 10% output from the laser amplifier down a computer-controlled optical delay line, then focusing into a 3 mm thick crystal of CaF_2, which was kept constantly moving to avoid laser damage. The residual 800 nm light was removed from the probe beam with an interference notch filter leaving an ~377–725 nm white light continuum. The probe beam was then focused into a stirred 2 mm quartz cuvette containing the solution to be measured. The transmitted probe beam was focused onto the end of a fiber-coupled spectrograph with a 1D, 2,048 pixel CCD array detector.

The excitation beam (330 nm, 0.16 μJ/pulse) was overlapped on the probe beam spot on the sample at an incident angle of ~5° after being optically chopped at 2.5 kHz using a synchronous chopper so that the spectrograph measured the transmitted probe beam alternatively as T_{ON} and T_{OFF}. The differential extinction $\Delta A = -\log_{10}(T_{ON}/T_{OFF})$ was calculated for each pair of pulses and was typically averaged over a 1 s interval for each delay time. Temporal chirp in the probe pulse was measured and corrected for by making a measurement on neat solvent; the resonant signal was then fitted for each probe wavelength to determine the zero-delay position between pump and probe.

Ultrafast photocurrent spectroscopy

Initially, pre-patterned co-planar Au contacts with a thickness of 100 nm, 10 μm electrode spacing, and 2 mm width were thermally evaporated on quartz substrates under a vacuum of 1×10^{-6} Torr. The active device area is 10 μm × 2 mm. One side of the contact is connected with a power supply (a Keithley 2400 SourceMeter), and another side of the contact is connected with a 70 GHz sampling oscilloscope with a 50 ohm resistance. The LDP NC device for photocurrent measurements is then fabricated by drop-casting the LDP NC solution (20 mg/mL) evenly onto the substrate. All photocurrent and I-V characteristics measurements were carried out in an optical cryostat-assisted vacuum environment. The charge carriers were

photogenerated under the ultrafast laser with a wavelength of 400 nm and 100 fs pulse. Temperature-dependent measurements span from 80 to 300 K.

Computational methods

Structure optimization and electronic calculations were both performed using a VASP code,[67–68] with the projector augmented wave potential method to describe the electron-ion interactions.[69] The PBE functional was used to describe the exchange and correlation interactions.[70] The band structures and DOS were calculated using the Heyd-Scuseria-Ernzerhof (HSE06)[71] hybrid functional. The splitting parameter (ω) was set to 0.2 and the component of Hartree-Fock (α = 0.25) were used to calculate electronic structures. The plane-wave cutoff energy was set to 500 eV, and the Γ-centered *k*-point meshes with *k*-spacing of 0.01 π $Å^{-1}$ were employed for DOS calculation. The lattice parameters and atomic positions were fully relaxed until the force on each atom was smaller than 0.02 eV/Å, and the convergence threshold of energy for the self-consistent was 10^{-5} eV.

As previously reported, magnetic ordering is crucial to obtaining a reasonable band structure for the LDP.[33,64] Both $Cs_4CuSb_2Cl_{12}$ and $Cs_4CdSb_2Cl_{12}$ in the trigonal- and monoclinic-phase systems were considered under paramagnetic, ferromagnetic (FM), and intra-layer antiferromagnetic (AFM) ordering, where the total energy difference per each atom with FM and AFM is shown in Figure S17. For $Cs_4Cd_{1-x}Cu_xSb_2Cl_{12}$, the AFM ordering resulted in the lower energy when the Cu concentration is larger than 0.50, which were selected for band structure and DOS calculation. The stable crystal structures defined as total energy difference (ΔE_m) per each atom under considering the magnetic ordering:

$$\Delta E_m = E_{T(FM)} - E_{T(AFM)},$$

where $E_{T(FM)}$ and $E_{T(AFM)}$ are the total energy $Cs_4Cd_{1-x}Cu_xSb_2Cl_{12}$ LDP with FM and AFM magnetic ordering.

The charge density difference was calculated by the following equation:

$$\Delta\rho(r) = \rho_{comp} - \rho_{Cs} - \rho_M - \rho_{Sb} - \rho_{Cl},$$

where ρ_{comp} is the charge density of $Cs_4Cd_{1-x}Cu_xSb_2Cl_{12}$ LDP, ρ_{Cs}, ρ_M, ρ_{Sb}, and ρ_{Cl} are the charge densities of Cs^+, M^{2+}(Cd, Cu), Sb^{3+}, and Cl^- ions isolated in $Cs_4Cd_{1-x}Cu_xSb_2Cl_{12}$ LDP, respectively. The blue and yellow areas represent the charge depletion and charge accumulation, respectively.

ELF has been proposed based on the second-order Taylor expansion of the spherically averaged pair density.[72] The ELF mapping can be directly applied to visualize bond characters between the ions.[73,74] A close-to-one ELF value suggests that the covalent bonds exist with a very high electron density between the two ions.

SUPPLEMENTAL INFORMATION

Supplemental information can be found online at https://doi.org/10.1016/j.matt.2021.07.018.

ACKNOWLEDGMENTS

O.C. acknowledges support from the National Science Foundation under the awards of DMR-1943930 and CMMI-1934314. T.C. is supported by the Open Graduate Education Program from Brown University. TEM, XRD, and EPR measurements were performed at the Electron Microscopy Facility in the Institute for Molecular and

Nanoscale Innovation (IMNI) at Brown University. This work was performed, in part, at the Center for Nanoscale Materials, a U.S. Department of Energy Office of Science User Facility, and supported by the U.S. Department of Energy, Office of Science, under contract no. DE-AC02-06CH11357. We acknowledge support from the National Science Foundation CBET Program under award no. 2025214. This research used resources of the Center for Functional Nanomaterials (CFN), which is a U.S. Department of Energy Office of Science User Facility, at Brookhaven National Laboratory under contract no. DE-SC0012704.

AUTHOR CONTRIBUTIONS

T.C. and O.C. conceived the idea and designed the study. T.C. performed the material synthesis, material characterization, and data analysis. W.S. contributed to the DFT calculations. D.J.G. and X.M. assisted with the TA studies. K.K. and J.G. helped with the photodetector fabrication and measurements. S.H. carried out the HR-TEM and STEM images. H.Y., N.J., Y.N., L.D., and J.S. helped with the experiments and discussion. T.C. and O.C. wrote the manuscript. All authors discussed the results and revised the manuscript.

DECLARATION OF INTERESTS

The authors declare no competing interests.

Received: May 9, 2021
Revised: June 28, 2021
Accepted: July 23, 2021
Published: August 19, 2021

REFERENCES

1. Swarnkar, A., Marshall, A.R., Sanehira, E.M., Chernomordik, B.D., Moore, D.T., Christians, J.A., Chakrabarti, T., and Luther, J.M. (2016). Quantum dot-induced phase stabilization of α-$CsPbI_3$ perovskite for high-efficiency photovoltaics. Science *354*, 92–95.

2. Que, M., Dai, Z., Yang, H., Zhu, H., Zong, Y., Que, W., Padture, N.P., Zhou, Y., and Chen, O. (2019). Quantum-dot-induced cesium-rich surface imparts enhanced stability to formamidinium lead iodide perovskite solar cells. ACS Energy Lett. *4*, 1970–1975.

3. Xing, J., Zhao, Y., Askerka, M., Quan, L.N., Gong, X., Zhao, W., Zhao, J., Tan, H., Long, G., Gao, L., et al. (2018). Color-stable highly luminescent sky-blue perovskite light-emitting diodes. Nat. Commun. *9*, 3541.

4. Han, D., Imran, M., Zhang, M., Chang, S., Wu, X.-g., Zhang, X., Tang, J., Wang, M., Ali, S., Li, X., et al. (2018). Efficient light-emitting diodes based on in situ fabricated $FAPbBr_3$ nanocrystals: the enhancing role of the ligand-assisted reprecipitation process. ACS Nano *12*, 8808–8816.

5. Song, J., Li, J., Li, X., Xu, L., Dong, Y., and Zeng, H. (2015). Quantum dot light-emitting diodes based on inorganic perovskite cesium lead halides ($CsPbX_3$). Adv. Mater. *27*, 7162–7167.

6. Chen, Q., Wu, J., Ou, X., Huang, B., Almutlaq, J., Zhumekenov, A.A., Guan, X., Han, S., Liang, L., Yi, Z., et al. (2018). All-inorganic perovskite nanocrystal scintillators. Nature *561*, 88–93.

7. Yakunin, S., Protesescu, L., Krieg, F., Bodnarchuk, M.I., Nedelcu, G., Humer, M., De Luca, G., Fiebig, M., Heiss, W., and Kovalenko, M.V. (2015). Low-threshold amplified spontaneous emission and lasing from colloidal nanocrystals of caesium lead halide perovskites. Nat. Commun. *6*, 8056.

8. Cai, T., Wang, J., Li, W., Hills-Kimball, K., Yang, H., Nagaoka, Y., Yuan, Y., Zia, R., and Chen, O. (2020). Mn^{2+}/Yb^{3+} codoped $CsPbCl_3$ perovskite nanocrystals with triple-wavelength emission for luminescent solar concentrators. Adv. Sci. *7*, 2001317.

9. Meinardi, F., Akkerman, Q.A., Bruni, F., Park, S., Mauri, M., Dang, Z., Manna, L., and Brovelli, S. (2017). Doped halide perovskite nanocrystals for reabsorption-free luminescent solar concentrators. ACS Energy Lett. *2*, 2368–2377.

10. Cohen, T.A., Milstein, T.J., Kroupa, D.M., MacKenzie, J.D., Luscombe, C.K., and Gamelin, D.R. (2019). Quantum-cutting Yb^{3+}-doped perovskite nanocrystals for monolithic bilayer luminescent solar concentrators. J. Mater. Chem. A *7*, 9279–9288.

11. Yuan, Y., Zhu, H., Hills-Kimball, K., Cai, T., Shi, W., Wei, Z., Yang, H., Candler, Y., Wang, P., He, J., et al. (2020). Stereoselective C-C oxidative coupling reactions photocatalyzed by zwitterionic ligand capped $CsPbBr_3$ perovskite quantum dots. Angew. Chem. Int. Ed. *59*, 22563–22569.

12. Xu, Y.-F., Yang, M.-Z., Chen, B.-X., Wang, X.-D., Chen, H.-Y., Kuang, D.-B., and Su, C.-Y. (2017). A $CsPbBr_3$ perovskite quantum dot/graphene oxide composite for photocatalytic CO_2 reduction. J. Am. Chem. Soc. *139*, 5660–5663.

13. Shamsi, J., Urban, A.S., Imran, M., De Trizio, L., and Manna, L. (2019). Metal halide perovskite nanocrystals: synthesis, post-synthesis modifications, and their optical properties. Chem. Rev. *119*, 3296–3348.

14. Huang, J., Lai, M., Lin, J., and Yang, P. (2018). Rich chemistry in inorganic halide perovskite nanostructures. Adv. Mater. *30*, 1802856.

15. Kovalenko, M.V., Protesescu, L., and Bodnarchuk, M.I. (2017). Properties and potential optoelectronic applications of lead halide perovskite nanocrystals. Science *358*, 745–750.

16. Giustino, F., and Snaith, H.J. (2016). Toward lead-free perovskite solar cells. ACS Energy Lett. *1*, 1233–1240.

17. Ning, W., and Gao, F. (2019). Structural and functional diversity in lead-free halide perovskite materials. Adv. Mater. *31*, 1900326.

18. Fan, Q., Biesold-McGee, G.V., Ma, J., Xu, Q., Pan, S., Peng, J., and Lin, Z. (2020). Lead-free halide perovskite nanocrystals: crystal structures, synthesis, stabilities, and optical properties. Angew. Chem. Int. Ed. *59*, 1030–1046.

19. Locardi, F., Cirignano, M., Baranov, D., Dang, Z., Prato, M., Drago, F., Ferretti, M., Pinchetti, V., Fanciulli, M., Brovelli, S., et al. (2018).

Colloidal synthesis of double perovskite $Cs_2AgInCl_6$ and Mn-doped $Cs_2AgInCl_6$ nanocrystals. J. Am. Chem. Soc. *140*, 12989–12995.

20. Slavney, A.H., Hu, T., Lindenberg, A.M., and Karunadasa, H.I. (2016). A bismuth-halide double perovskite with long carrier recombination lifetime for photovoltaic applications. J. Am. Chem. Soc. *138*, 2138–2141.

21. Creutz, S.E., Crites, E.N., De Siena, M.C., and Gamelin, D.R. (2018). Colloidal nanocrystals of lead-free double-perovskite (elpasolite) semiconductors: synthesis and anion exchange to access new materials. Nano Lett. *18*, 1118–1123.

22. Bekenstein, Y., Dahl, J.C., Huang, J., Osowiecki, W.T., Swabeck, J.K., Chan, E.M., Yang, P., and Alivisatos, A.P. (2018). The making and breaking of lead-free double perovskite nanocrystals of cesium silver-bismuth halide compositions. Nano Lett. *18*, 3502–3508.

23. Yang, B., Hong, F., Chen, J., Tang, Y., Yang, L., Sang, Y., Xia, X., Guo, J., He, H., Yang, S., et al. (2019). Colloidal synthesis and charge-carrier dynamics of $Cs_2AgSb_{1-y}Bi_yX_6$ (X: Br, Cl; $0 \leq y \leq 1$) double perovskite nanocrystals. Angew. Chem. Int. Ed. *58*, 2278–2283.

24. Arfin, H., Kaur, J., Sheikh, T., Chakraborty, S., and Nag, A. (2020). Bi^{3+}-Er^{3+} and Bi^{3+}-Yb^{3+} codoped $Cs_2AgInCl_6$ double perovskite near-infrared emitters. Angew. Chem. Int. Ed. *59*, 11307–11311.

25. Chen, M., Ju, M.-G., Carl, A.D., Zong, Y., Grimm, R.L., Gu, J., Zeng, X.C., Zhou, Y., and Padture, N.P. (2018). Cesium titanium(IV) bromide thin films based stable lead-free perovskite solar cells. Joule *2*, 558–570.

26. Zhou, W., Han, P., Zhang, X., Zheng, D., Yang, S., Yang, Y., Luo, C., Yang, B., Hong, F., Wei, D., et al. (2020). Lead-free small-bandgap $Cs_2CuSbCl_6$ double perovskite nanocrystals. J. Phys. Chem. Lett. *11*, 6463–6467.

27. Yang, B., Chen, J., Hong, F., Mao, X., Zheng, K., Yang, S., Li, Y., Pullerits, T., Deng, W., and Han, K. (2017). Lead-free, air-stable All-inorganic cesium bismuth halide perovskite nanocrystals. Angew. Chem. Int. Ed. *56*, 12471–12475.

28. Zhang, J., Yang, Y., Deng, H., Farooq, U., Yang, X., Khan, J., Tang, J., and Song, H. (2017). High quantum yield blue emission from lead-free inorganic antimony halide perovskite colloidal quantum dots. ACS Nano *11*, 9294–9302.

29. Yang, H., Cai, T., Liu, E., Hills-Kimball, K., Gao, J., and Chen, O. (2019). Synthesis and transformation of zero-dimensional Cs_3BiX_6 (X = Cl, Br) perovskite-analogue nanocrystals. Nano Res. *13*, 282–291.

30. Shi, W., Cai, T., Wang, Z., and Chen, O. (2020). The effects of monovalent metal cations on the crystal and electronic structures of Cs_2MBiCl_6 (M = Ag, Cu, Na, K, Rb, and Cs) perovskites. J. Chem. Phys. *153*, 141101.

31. Vargas, B., Ramos, E., Perez-Gutierrez, E., Alonso, J.C., and Solis-Ibarra, D. (2017). A direct bandgap copper-antimony halide perovskite. J. Am. Chem. Soc. *139*, 9116–9119.

32. Vargas, B., Rodrıguez-López, G., and Solis-Ibarra, D. (2020). The emergence of halide layered double perovskites. ACS Energy Lett. *5*, 3591–3608.

33. Cai, T., Shi, W., Hwang, S., Kobbekaduwa, K., Nagaoka, Y., Yang, H., Hills-Kimball, K., Zhu, H., Wang, J., Wang, Z., et al. (2020). Lead-free $Cs_4CuSb_2Cl_{12}$ layered double perovskite nanocrystals. J. Am. Chem. Soc. *142*, 11927–11936.

34. Wei, J.-H., Liao, J.-F., Wang, X.-D., Zhou, L., Jiang, Y., and Kuang, D.-B. (2020). All-inorganic lead-free heterometallic $Cs_4MnBi_2Cl_{12}$ perovskite single crystal with highly efficient orange emission. Matter *3*, 892–903.

35. Bai, T., Yang, B., Chen, J., Zheng, D., Tang, Z., Wang, X., Zhao, Y., Lu, R., and Han, K. (2021). Efficient luminescent halide quadruple-perovskite nanocrystals via trap-engineering for highly sensitive photodetectors. Adv. Mater. *33*, 2007215.

36. Gray, M.B., Majher, J.D., Holzapfel, N.P., and Woodward, P.M. (2021). Exploring the stability of mixed-halide vacancy-ordered quadruple perovskites. Chem. Mater. *33*, 2165–2172.

37. Holzapfel, N.P., Majher, J.D., Strom, T.A., Moore, C.E., and Woodward, P.M. (2020). $Cs4Cd_{1-x}Mn_xBi_2Cl_{12}$—a vacancy-ordered halide perovskite phosphor with high-efficiency orange-red emission. Chem. Mater. *32*, 3510–3516.

38. Vargas, B., Reyes-Castillo, D.T., Coutino-Gonzalez, E., Sánchez-Aké, C., Ramos, C., Falcony, C., and Solis-Ibarra, D. (2020). Enhanced luminescence and mechanistic studies on layered double-perovskite phosphors: $Cs_4Cd_{1-x}Mn_xBi_2Cl_{12}$. Chem. Mater. *32*, 9307–9315.

39. Vargas, B., Torres-Cadena, R., Rodríguez-Hernández, J., Gembicky, M., Xie, H., Jiménez-Mier, J., Liu, Y.-S., Menéndez-Proupin, E., Dunbar, K.R., Lopez, N., et al. (2018). Optical, electronic, and magnetic engineering of <111> layered halide perovskites. Chem. Mater. *30*, 5315–5321.

40. Vargas, B., Coutino-Gonzalez, E., Ovalle-Encinia, O., Sanchez-Ake, C., and Solis-Ibarra, D. (2020). Efficient emission in halide layered double perovskites: the role of Sb^{3+} substitution in $Cs_4Cd_{1-x}Mn_xBi_2Cl_{12}$ phosphors. J. Phys. Chem. Lett. *11*, 10362–10367.

41. Singhal, N., Chakraborty, R., Ghosh, P., and Nag, A. (2018). Low-bandgap $Cs_4CuSb_2Cl_{12}$ layered double perovskite: synthesis, reversible thermal changes, and magnetic interaction. Chem. Asian J. *13*, 2085–2092.

42. Vargas, B., Torres-Cadena, R., Reyes-Castillo, D.T., Rodríguez-Hernández, J., Gembicky, M., Menéndez-Proupin, E., and Solis-Ibarra, D. (2019). Chemical diversity in lead-free, layered double perovskites: a combined experimental and computational approach. Chem. Mater. *32*, 424–429.

43. Lin, Y.P., Hu, S., Xia, B., Fan, K.Q., Gong, L.K., Kong, J.T., Huang, X.Y., Xiao, Z., and Du, K.Z. (2019). Material design and optoelectronic properties of three-dimensional quadruple perovskite halides. J. Phys. Chem. Lett. *10*, 5219–5225.

44. Tang, G., Xiao, Z., Hosono, H., Kamiya, T., Fang, D., and Hong, J. (2018). Layered halide double perovskites $Cs_{3+n}M(II)_nSb_2X_{9+3n}$ (M = Sn, Ge) for photovoltaic applications. J. Phys. Chem. Lett. *9*, 43–48.

45. Han, D., Zhang, T., and Chen, S. (2020). High-throughput first-principles screening of layered magnetic double perovskites $Cs_4MSb_2X_{12}$ for spintronic applications. J. Phys. Condens. Matter. *32*, 225705.

46. Wang, X.D., Miao, N.H., Liao, J.F., Li, W.Q., Xie, Y., Chen, J., Sun, Z.M., Chen, H.Y., and Kuang, D.B. (2019). The top-down synthesis of single-layered $Cs_4CuSb_2Cl_{12}$ halide perovskite nanocrystals for photoelectrochemical application. Nanoscale *11*, 5180–5187.

47. Xu, J., Xu, C., Liu, J.-B., Bellaiche, L., Xiang, H., Liu, B.-X., and Huang, B. (2019). Prediction of room-temperature half-metallicity in layered halide double perovskites. NPJ Comput. Mater. *5*, 114.

48. Tran, T.T., Pocs, C.A., Zhang, Y., Winiarski, M.J., Sun, J., Lee, M., and McQueen, T.M. (2020). Spinon excitations in the quasi-one-dimensional S=1/2 chain compound $Cs_4CuSb_2Cl_{12}$. Phys. Rev. B *101*, 235107.

49. Yang, H., Shi, W., Cai, T., Hills-Kimball, K., Liu, Z., Dube, L., and Chen, O. (2020). Synthesis of lead-free $Cs_4(Cd_{1-x}Mn_x)Bi_2Cl_{12}$ ($0 \leq x \leq 1$) layered double perovskite nanocrystals with controlled Mn-Mn coupling interaction. Nanoscale *12*, 23191–23199.

50. Hu, S., Xia, B., Lin, Y.-P., Katase, T., Fujioka, J., Kamiya, T., Hosono, H., Du, K.-Z., and Xiao, Z. (2020). p-Type transparent quadruple perovskite halide conductors: fact or fiction? Adv. Funct. Mater. *30*, 1909906.

51. Xu, J., Liu, J.-B., Wang, J., Liu, B.-X., and Huang, B. (2018). Prediction of novel p-type transparent conductors in layered double perovskites: a first-principles study. Adv. Funct. Mater. *28*, 1800332.

52. Xu, J., Liu, J.-B., Wang, J., Liu, B.-X., and Huang, B. (2020). Response to comment on "prediction of novel p-type transparent conductors in layered double perovskites: a first-principles study". Adv. Funct. Mater. *30*, 2003149.

53. Imran, M., Caligiuri, V., Wang, M., Goldoni, L., Prato, M., Krahne, R., De Trizio, L., and Manna, L. (2018). Benzoyl halides as alternative precursors for the colloidal synthesis of lead-based halide perovskite nanocrystals. J. Am. Chem. Soc. *140*, 2656–2664.

54. Cai, T., Yang, H., Hills-Kimball, K., Song, J.-P., Zhu, H., Hofman, E., Zheng, W., Rubenstein, B.M., and Chen, O. (2018). Synthesis of all-inorganic Cd-doped $CsPbCl_3$ perovskite nanocrystals with dual-wavelength emission. J. Phys. Chem. Lett. *9*, 7079–7084.

55. Tauc, J., Grigorovici, R., and Vancu, A. (1966). Optical properties and electronic structure of amorphous germanium. Phys. Status. Solidi. (B) *15*, 627–637.

56. Yang, B., and Han, K. (2019). Charge-carrier dynamics of lead-free halide perovskite nanocrystals. Acc. Chem. Res. *52*, 3188–3198.

57. Holder, C.F., and Schaak, R.E. (2019). Tutorial on powder X-ray diffraction for characterizing nanoscale materials. ACS Nano *13*, 7359–7365.

58. Godiksen, A., Vennestrøm, P.N.R., Rasmussen, S.B., and Mossin, S. (2016). Identification and quantification of copper sites in zeolites by electron paramagnetic resonance spectroscopy. Top. Catal. *60*, 13–29.

59. Wagner, E.P., Gronborg, K.C., Ghosh, S., and Saxena, S. (2019). An undergraduate experiment to explore Cu(II) coordination environment in multihistidine compounds through electron spin resonance spectroscopy. J. Chem. Educ. *96*, 1752–1759.

60. Karmakar, A., Dodd, M.S., Agnihotri, S., Ravera, E., and Michaelis, V.K. (2018). Cu(II)-doped $Cs_2SbAgCl_6$ double perovskite: a lead-free, low-bandgap material. Chem. Mater. *30*, 8280–8290.

61. Liao, Q., Chen, J., Zhou, L., Wei, T., Zhang, L., Chen, D., Huang, F., Pang, Q., and Zhang, J.Z. (2020). Bandgap engineering of lead-free double perovskite $Cs_2AgInCl_6$ nanocrystals via Cu^{2+}-doping. J. Phys. Chem. Lett. *11*, 8392–8398.

62. Himmetoglu, B., Wentzcovitch, R.M., and Cococcioni, M. (2011). First-principles study of electronic and structural properties of CuO. Phys. Rev. B *84*, 115108.

63. Heinemann, M., Eifert, B., and Heiliger, C. (2013). Band structure and phase stability of the copper oxides Cu_2O, CuO, and Cu_4O_3. Phys. Rev. B *87*, 115111.

64. Wang, X., Meng, W., Xiao, Z., Wang, J., Mitzi, D., and Yan, Y. (2017). First-principles understanding of the electronic band structure of copper-antimony halide perovskite: the effect of magnetic ordering. arXiv, 1707.09539.

65. Yang, B., Mao, X., Hong, F., Meng, W., Tang, Y., Xia, X., Yang, S., Deng, W., and Han, K. (2018). Lead-free direct band gap double-perovskite nanocrystals with bright dual-color emission. J. Am. Chem. Soc. *140*, 17001–17006.

66. Klimov, V.I. (2000). Optical nonlinearities and ultrafast carrier dynamics in semiconductor nanocrystals. J. Phys. Chem. B *104*, 6112–6123.

67. Kresse, G., and Joubert, D. (1999). From ultrasoft pseudopotentials to the projector augmented-wave method. Phys. Rev. B *59*, 1758–1775.

68. Kresse, G., and Furthmüller, J. (1996). Efficient iterative schemes for ab initio total-energy calculations using a plane-wave basis set. Phys. Rev. B *54*, 11169–11186.

69. Blöchl, P.E. (1994). Projector augmented-wave method. Phys. Rev. B *50*, 17953–17979.

70. Perdew, J.P., Burke, K., and Ernzerhof, M. (1996). Generalized gradient approximation made simple. Phys. Rev. Lett. *77*, 3865–3868.

71. Heyd, J., Scuseria, G.E., and Ernzerhof, M. (2003). Hybrid functionals based on a screened Coulomb potential. J. Chem.Phys. *118*, 8207–8215.

72. Becke, A.D., and Edgecombe, K.E. (1990). A simple measure of electron localization in atomic and molecular systems. J. Chem.Phys. *92*, 5397–5403.

73. Savin, A., Nesper, R., Wengert, S., and Fässler, T.F. (1997). ELF: the electron localization function. Angew. Chem. Int. Ed. *36*, 1808–1832.

74. de Silva, P., Korchowiec, J., and Wesolowski, T.A. (2012). Revealing the bonding pattern from the molecular electron density using single exponential decay detector: an orbital-free alternative to the electron localization function. ChemPhysChem *13*, 3462–3465.